JOURNAL OF APPLIED PHYSICS **114**, 083109 (2013)

The role of plasma evolution and photon transport in optimizing future advanced lithography sources

Tatyana Sizyuk and Ahmed Hassanein
Center for Materials Under Extreme Environment, School of Nuclear Engineering, Purdue University, West Lafayette, Indiana 47907, USA

(Received 22 March 2013; accepted 13 August 2013; published online 28 August 2013)

Laser produced plasma (LPP) sources for extreme ultraviolet (EUV) photons are currently based on using small liquid tin droplets as target that has many advantages including generation of stable continuous targets at high repetition rate, larger photons collection angle, and reduced contamination and damage to the optical mirror collection system from plasma debris and energetic particles. The ideal target is to generate a source of maximum EUV radiation output and collection in the 13.5 nm range with minimum atomic debris. Based on recent experimental results and our modeling predictions, the smallest efficient droplets are of diameters in the range of 20–30 μm in LPP devices with dual-beam technique. Such devices can produce EUV sources with conversion efficiency around 3% and with collected EUV power of 190 W or more that can satisfy current requirements for high volume manufacturing. One of the most important characteristics of these devices is in the low amount of atomic debris produced due to the small initial mass of droplets and the significant vaporization rate during the pre-pulse stage. In this study, we analyzed in detail plasma evolution processes in LPP systems using small spherical tin targets to predict the optimum droplet size yielding maximum EUV output. We identified several important processes during laser-plasma interaction that can affect conditions for optimum EUV photons generation and collection. The importance and accurate description of modeling these physical processes increase with the decrease in target size and its simulation domain. *© 2013 AIP Publishing LLC*. [http://dx.doi.org/10.1063/1.4819439]

I. INTRODUCTION

Intense photon beams at the 13.5 nm extreme ultraviolet (EUV) range are proposed for the next generation lithography chip manufacturing technology. Laser produced plasma (LPP) devices are being developed to generate the required EUV photon source for nanolithography. Advanced computer simulation of LPP can be important tool for designing and optimizing LPP devices and can significantly reduce the cost and the time of conducting extensive experiments. However, accurate simulation of LPP devices for extreme ultraviolet lithography (EUVL) requires advanced multidimensional physical models and numerical methods. Modeling of such devices should include description of all laser/target interaction processes. These processes include laser photons interaction with target material in all phases, thermal conduction in material and in plasma, vaporization, hydrodynamic evolution of target vapor and plasma, ionization, plasma radiation, and details of photon transport in these media. We studied the influence and the importance of various processes and models, implemented in our comprehensive HEIGHTS package, on plasma evolution dynamics and as result on EUV source intensity, location, and size.

Plasmas in intense LPP sources have high gradients of radiation energy density at small spatial lengths and require special treatment. Therefore, accurate physical/mathematical models and appropriate numerical methods should be implemented and carefully benchmarked for correct calculation of plasma evolution, opacity, photons generation, and their transport and distribution. One of the most important processes in understanding plasma evolution and EUV source generation and location is photon transport in such complex plasma environment. We have implemented and compared two separate methods for calculating radiation transport, i.e., direct integration of the radiation transport equation along photon path and Monte Carlo models with several novel weight factors to enhance the accuracy and the speed of calculations. These two independent methods agree well with each other and highlight the importance of accurate full 3D solution of radiation transport equations for the correct simulation of LPP sources.[1] Detailed description of laser energy absorption and dynamics of target vaporization are also quite important for various laser/plasma interaction regimes in EUVL devices. Hydrodynamic effects during plasma evolution and confinement can significantly influence EUV emission, which usually follows laser intensity profile in ideal LPP conditions.

The effect of models detail for the above mentioned processes on resulting conversion efficiency (CE) of LPP sources for EUV photons production is critically evident in systems using small, 10–50 μm, spherical targets. The desire for the smallest possible target is based on the requirement for longer chamber components lifetime mainly the mirrors collecting system.[2] Such mass-limited targets allow reducing debris fluence to the optical system preventing contamination and surface damage. However, small size of target leads to reducing laser spot size and, as consequence, a significant decrease in CE of laser energy to EUV useful photons.[3] While such decrease is less pronounced in the case of Nd:YAG laser, the CE of the CO_2 laser decreases by several times in comparison to planar targets where larger laser spots can be used. Utilizing the pre-pulse laser with shorter wavelength allows preparing plasma for the main CO_2 pulse with larger spot size and such dual-beam devices provide significant increase in CE making it comparable or even higher than the CE from planar targets.[4–6] We evaluated using our HEIGHTS simulation package the CE of dual-beam systems with various droplet sizes, starting from 10 μm, and our results indicated that the smallest efficient droplets should be in the range of 20–30 μm.[7,8]

The purpose of this study is to investigate the differences in EUV photons production for different geometries and target conditions that can explain recent experimental results and then demonstrate ways for future target optimizations in these regards. We also studied the influence of different processes on EUV source characteristics for various pre-plasma conditions and main laser parameters. Our analysis is based on extensive benchmarking of the detailed models implemented in the integrated HEIGHTS package with our CMUXE experimental results[9–11] as well as results of other groups working in EUVL area.[12] All simulation results for the CE in current work correspond to the EUV photons output in the 13.5% ± 1% range collected in 2π sr.

II. MODELING OF MAJOR PROCESSES IN LPP

Plasma characteristics and their spatial and temporal distribution in LPP devices for the EUVL relevant laser parameters are determined by these main processes: laser energy deposition, target evolution thermodynamics and hydrodynamics, resulting vapor ionization and plasma hydrodynamics, thermal conduction, and radiation transport. The expanded general MHD equation set in a two-temperature approximation used in HEIGHTS package is given by

$$\begin{cases} \dfrac{\partial \rho}{\partial t} + \nabla \cdot (\rho \mathbf{v}) = 0 \\ \dfrac{\partial \rho \mathbf{v}}{\partial t} + \nabla \cdot \left(\rho \mathbf{v}\mathbf{v} + p_{tot} - \dfrac{\mathbf{B}\mathbf{B}}{4\pi\mu} \right) = -\dfrac{1}{4\pi\mu}\mathbf{B}(\nabla \cdot \mathbf{B}) \\ \dfrac{\partial e_{tot}}{\partial t} + \nabla \cdot \left[\mathbf{v}(e_{tot} + p_{tot}) - \dfrac{1}{4\pi\mu}(\mathbf{v} \cdot \mathbf{B}) \cdot \mathbf{B} + \dfrac{c^2 \eta}{16\pi^2\mu^2}(\nabla \times \mathbf{B}) \times \mathbf{B} - \lambda_e \nabla T_e - \lambda_i \nabla T_i - \mathbf{S}_{rad} \right] = Q_{las} - \dfrac{1}{4\pi\mu}(\mathbf{v} \cdot \mathbf{B}) \cdot (\nabla \cdot \mathbf{B}) \\ \dfrac{\partial e_i}{\partial t} + \nabla \cdot [\mathbf{v}(e_i + p_i) - \lambda_i \nabla T_i] = Q_{ei} \\ \dfrac{\partial \mathbf{B}}{\partial t} + \nabla \cdot (\mathbf{v}\mathbf{B} - \mathbf{B}\mathbf{v}) + \dfrac{c^2}{4\pi\mu} \nabla \times (\eta \nabla \times \mathbf{B}) + \dfrac{c k_B}{e n_e} \nabla n_e \times \nabla T_e = -\mathbf{v}(\nabla \cdot \mathbf{B}), \end{cases} \tag{1}$$

where ρ is the density of plasma; $\mathbf{v}$ is the velocity of plasma; p_{tot} includes the hydrodynamic and magnetic parts of the pressure: $p_{tot} = p_e + p_i + \frac{B^2}{8\pi\mu}$; e_{tot} is the total energy, which includes the hydrodynamic part, $e_h = e_e + e_i + e_{kin}$, where e_e and e_i are for the electronic component and for the ion component correspondently, $e_{kin} = \frac{\rho v^2}{2}$ is the kinetic energy of the plasma, and the magnetic part $e_m = \frac{B^2}{8\pi\mu}$. The radiation transport process is represented here as flux $\mathbf{S}_{rad}$ and the laser heating source as Q_{las}. Components $\frac{c^2\eta}{16\pi^2\mu^2}(\nabla \times \mathbf{B}) \times \mathbf{B}$ and $\frac{c^2}{4\pi\mu}\nabla \times (\eta \nabla \times \mathbf{B})$ describe magnetic diffusion processes, where η is the resistivity and μ is the magnetic permeability. The thermal conduction in the plasma is considered as the combined result of the electron $\lambda_e \nabla T_e$ and ion $\lambda_i \nabla T_i$ conductivity, where λ is the conductivity coefficient and T is the temperature. Also taken into account is the energy interchange between electrons and ions Q_{ei} and the thermally generated magnetic field $\frac{ck_B}{en_e}\nabla n_e \times \nabla T_e$.[13] Here, n_e is electron concentration; c is the speed of light; e is the electron charge; and k_B is the Boltzmann constant.

Equation (1) is a mixed hyperbolic–parabolic representation. A powerful approach that HEIGHTS utilizes for the solution of these equations is the splitting methods, which involve decoupling the full model into a separate component for each process, employing specialized numerical methods to solve each component, and coupling the resulting solutions.[1]

Modeling of the entire evolution of LPP in HEIGHTS package utilizes the most suited numerical and physical models for LPP plasma, e.g., weighted Monte Carlo methods for laser deposition and plasma radiation, phase change and thermal vaporization based on surface atoms kinetics modeling,[14] Eulerian/Lagrangian description of plasma hydrodynamic evolution in multidimensional finite volume approximation, and implicit methods for plasma thermal conduction and magnetic diffusion with sparse linear equations solvers.

Plasma thermodynamic properties and optical coefficients are calculated using the self-consistent Hartree-Fock-Slater (HFS) model implemented in HEIGHTS.[15] The populations of atomic levels, ionization balance, and the ion and electron plasma concentrations are obtained based on the collisional-radiative equilibrium (CRE) approximation. Tabulated plasma properties and optical coefficients for wide range of temperatures and densities are used during the simulation of whole cycle of plasma evolution in LPP. Spatial attention was paid to the accuracy and details of plasma optical coefficients in the EUV range.[16] Based on HEIGHTS calculations, the five ions starting from Sn^{+9} to Sn^{+13} contribute to the EUV emission near 13 nm in Sn plasma, which is considered as the main source of radiation in this region.[3] Detailed description of models for calculation of atomic data and plasma properties is given elsewhere.[15]

HEIGHTS package includes models in 3D coordinate system for vapor/plasma hydrodynamics, for magnetic diffusion, and for heat transfer in plasma and in the target; 3D Monte Carlo simulations of plasma and laser photon transport. Models were tested and dependence of results on geometry, mesh size, particle number, and energy spectra resolution was analyzed. Based on this models verification together with extensive benchmarking, we found the best solutions for modeling different regimes and device configurations.

III. LASER ENERGY ABSORPTION, REFLECTION, AND REABSORPTION

Models for self-consistent description of laser energy absorption combined with target material vaporization are critical parts in the simulation of LPP systems. This is more pronounced in the case of lower laser intensities, i.e., 10^8–10^{10} W/cm^2, and in plasma development from small targets with non-flat geometries. This becomes important because of the complex hydrodynamic flow near the target surfaces where one should take into account various energy input from laser radiation, i.e., absorption/reflection in solid/liquid target, in target vapor, and in evolving plasma layer. The entire processes should consider various phases of transition from the laser interaction with material only (in vacuum chamber) to preferential absorption in the developed hot plasma. The CE of EUV sources depends on many parameters including the initial target preparation stage as well as the efficiency of laser energy absorption in the developed plasma plume. Current optimum target preparation usually involves the use of dual laser pulse system, an initial low energy pulse to start generation of target plasma, and then followed by a main pulse with larger spot to produce more efficient EUV photons. In this regard, taking into account laser photons absorption after reflection from the target surface can be very important in determining the overall CE of the source.

For precise modeling of laser target interaction processes, we implemented experimental data of the optical properties for laser reflection from liquid tin, verified with theoretical calculations;[17] then, modeled laser absorption in vapor based on the main feature of collision-induced absorption—quadratic dependence on density, and the inverse bremsstrahlung absorption was used for simulation of laser photons interaction with plasma.

Figure 1 demonstrates the efficiency of the CO_2 laser energy absorption on the surface and in the developed plasma from small 30-μm droplet. Figure 2 shows the same but for the pre-plasma created by low intensity Nd:YAG pre-pulse from same size droplet after 450 ns expansion. Only 50% of laser energy was absorbed by the target and by plasma in LPP without pre-pulse, while in device with pre-plasma about 90% of laser photons was utilized. We should note that we used the 266 nm wavelength laser for the pre-pulse with low intensity of 2.5×10^{10} W/cm^2 and 10 ns pulse duration. Laser with these parameters vaporized most of the droplet. This allowed accurate simulation of vapor/plasma expansion before the main CO_2 pulse and without concerns about target fragmentation processes. The CEs stated in Figs. 1 and 2 labels are the optimized values for these systems.

More than half of the initial laser energy was reflected from the surface of small spherical targets (Fig. 1)—corresponding to the sum of both green and gray plots. However, during the increase in laser intensity with time, that caused increase in plasma density and temperature, many of the reflected photons were absorbed in the evolving plasma.

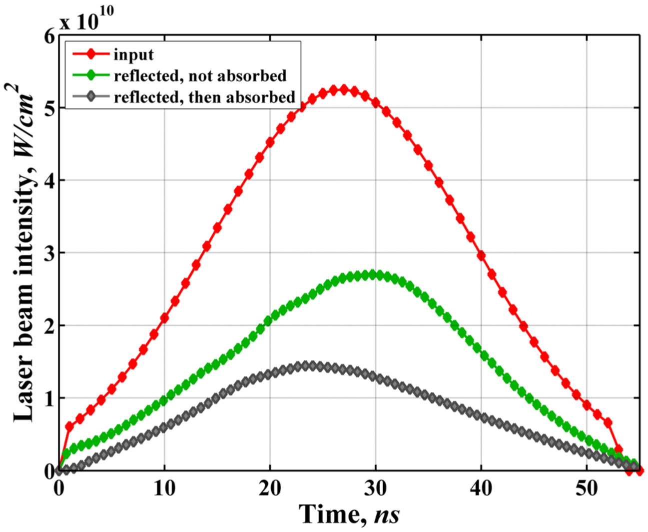

FIG. 1. CO_2 laser energy absorption in material and in plasma from 30 μm droplet without pre-pulse –0.45% CE. Gray curve shows laser energy that was absorbed in plasma after reflection and green curve shows reflected laser energy that was not absorbed in evolving plasma.

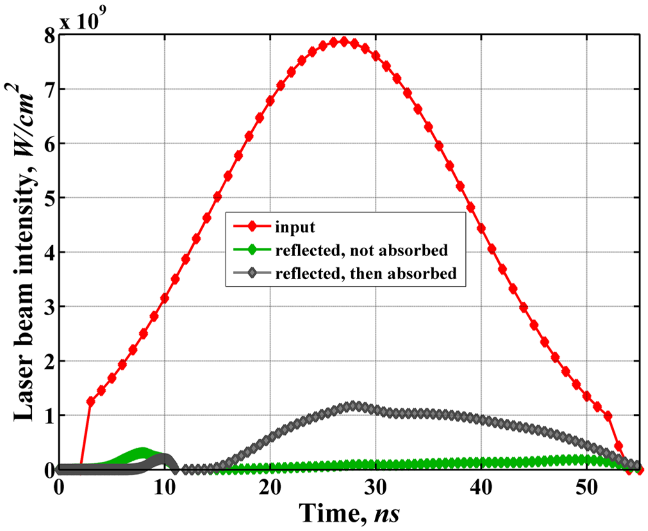

FIG. 2. CO_2 laser energy absorption in pre-plasma created from 30 μm droplet by 266 nm laser and expanded during 450 ns–2.9% CE. Gray curve shows laser energy that was absorbed in plasma after reflection and green curve shows reflected laser energy that was not absorbed in evolving plasma.

When laser intensity starts to decrease, plasma above the surface begins to cool down and density of the plasma is subsequently reduced because of plasma expansion and the flow around droplet as well as lower evaporation rate in comparison with the beginning of laser pulse. These processes resulted in lower absorption of the reflected photons that can affect and be an indicator for lower LPP source efficiency. It was shown in our previous analysis of comparing plasma behavior in LPP with planar and spherical targets using the same laser parameters[7] that the laser absorption rate in plasma for planar target is 30% higher than from droplets. The CE of the planar target is two times larger in these cases. Modeling and implementation of laser photons absorption in plasma after reflection from the target can, therefore, significantly affect the final EUV collected power. Not taking into account this effect during laser-target/plasma interaction of these small droplets and small spot sizes significantly decreased the CE of this system of more than three times.

The time history of laser photons reflection and absorption after reflection during reheating of the pre-plasma by the main CO_2 laser is shown in Fig. 2. This illustrates the evolution of processes in pre-plasma starting from cold vapor/plasma where almost all photons were transmitted through matter. Reflection processes and following absorption after reflection correspond to the time of the intense interaction of laser photons with the remained non-vaporized part of the droplet. When laser intensity increased almost all photons were absorbed in the heated pre-plasma zone, far from the target surface. Then, due to the hot plasma dynamics and compression toward the target position (specificity due to CO_2 laser interaction with pre-plasma), area of preferential laser absorption also moved closer toward the target. Laser photons then had more interactions with target surface and as a consequence more reflected and reabsorbed photons occurred at this time.

Figures 3 and 4 stress these points and illustrate areas of accumulated laser energy absorption during the pulse with the corresponding location of droplets.

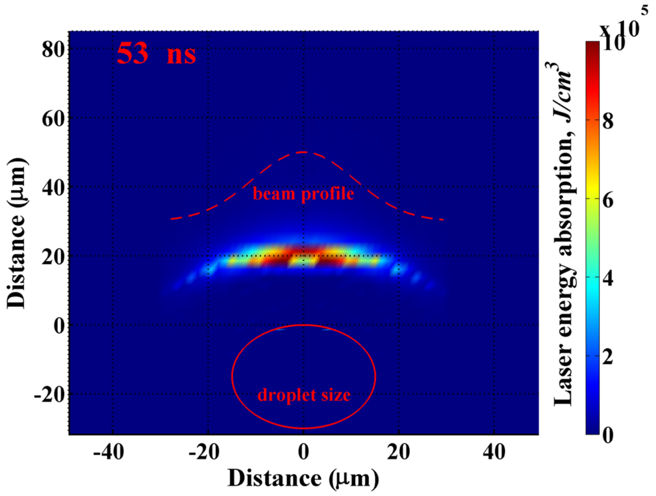

FIG. 3. CO_2 laser energy absorption during pulse in material and plasma from 30 μm droplet without pre-pulse. Laser pulse was used with 30 ns (FWHM) duration and 30 μm (FWHM) spot size.

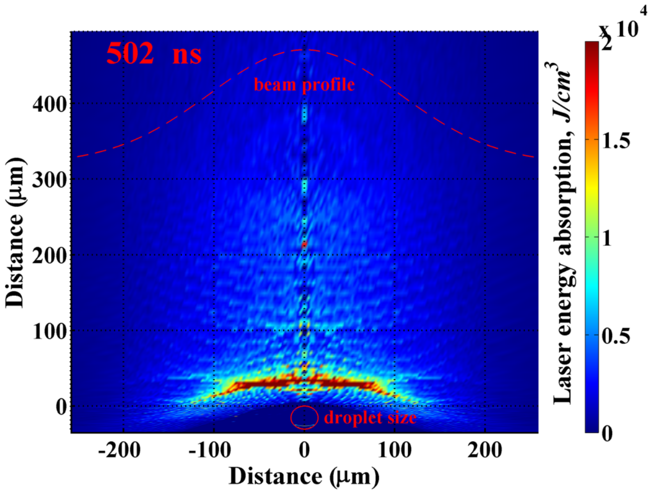

FIG. 4. CO_2 laser energy absorption during pulse in pre-plasma created from 30 μm droplet by 266 nm laser and expanded during 450 ns. Laser pulse was used with 30 ns (FWHM) duration and 300 μm (FWHM) spot size.

IV. RADIATION TRANSPORT DURING PLASMA EVOLUTION

Self-consistent modeling of processes during target ablation is necessary for accurate predictions of plasma evolution and CE calculation. Initially, laser photons start to heat the target surface initiating target vaporization. Subsequent laser interaction with the developed vapor/plasma results in reducing laser penetration to the target; however, it initiates heating of the target from plasma radiation. Thermal conduction in plasma redistributes energy of absorbed laser photons that also affects dynamics of target vaporization through the radiation from the warm plasma around the target surface. Hydrodynamic effects such as spherical expansion of plume and plasma motion around the droplet result in density redistribution that changes dynamics of laser photons absorption as well as plasma radiation emission and absorption in evolving plasma and on the target surface.

Radiation transport is one of the main mechanisms responsible for target heating and vaporization. Figures 5 and 6 show simulation results of tin foil ablation by CO_2 and Nd:YAG laser with the same pulse parameters, i.e.,

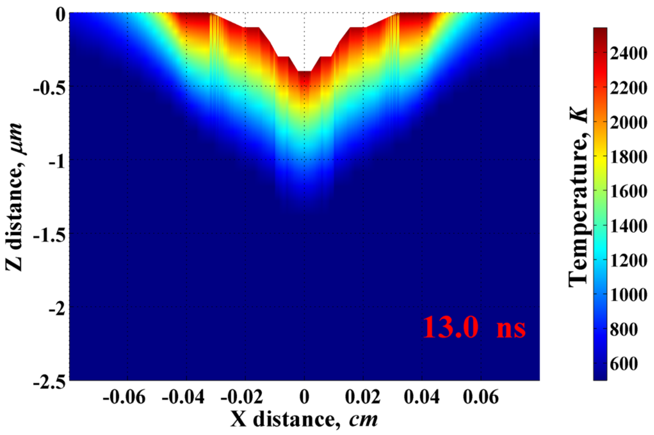

FIG. 5. Sn erosion by the CO_2 laser with 100 μm spot and 10^{11} W/cm^2 intensity.

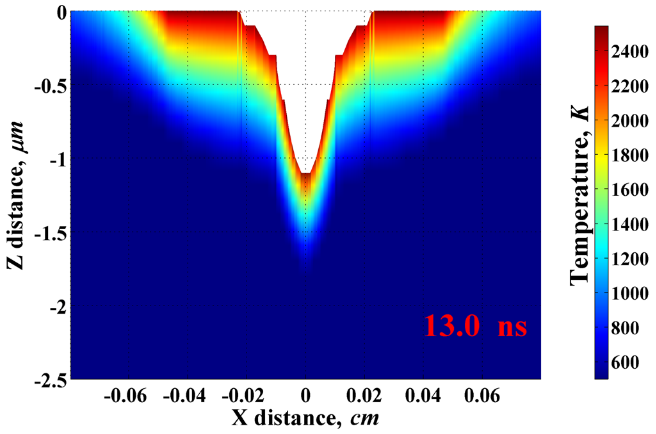

FIG. 6. Sn erosion by the Nd:YAG (1064 nm) laser with 100 μm spot and 10^{11} W/cm^2 intensity.

10^{11} W/cm^2 intensity, 100 μm spot, and 10 ns duration. This intensity of lasers created plasmas with temperatures up to 65 eV in case of Nd:YAG and up to 120 eV by the CO$_2$ laser. Most of laser photons were absorbed in the hot plasma. The temperature distributions in the target and erosion profile are attributed to the plasma radiation. Temperature profile on the surface demonstrates processes of plume expansion in LPP source with planar target, i.e., with denser plasma at the center of laser spot and with hotter less dense plasma correspondent to the wings of surface temperature.

Figures 7 and 8 show the corresponding predicted energy density to the target surface from the direct laser irradiation and from generated plasma integrated in time. These plots together with figures for the temperature distribution illustrate the strong effect of plasma shielding of laser photons as well as the role of plasma radiation for the considered laser beam intensity for both CO$_2$ and Nd:YAG lasers. Figures 7 and 8 reflect plasma evolution processes in LPP devices with relatively high laser intensity. The extensive evaporation of the target in the central spot area resulted in motion of vapor/plasma flow from the crater. On the other hand, compression of plasma around the center area of the laser spot initiates free expansion of vapor/plasma around the spot. Radiation fluxes from this plasma heat the target surface in the location outside of laser area. However, due to less intensity but longer duration of this peripheral radiation as well as deposited energy dissipation due to thermal conduction, plasma radiation did not cause significant surface evaporation at this location in contrast to the conditions at the spot center.

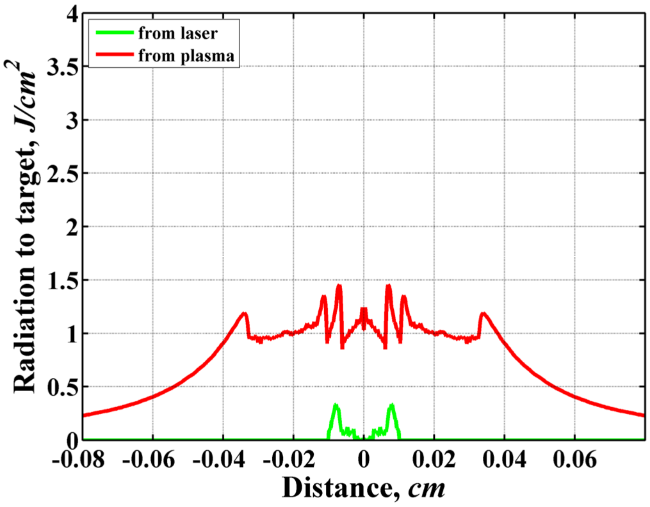

FIG. 7. Radiation to the target from laser and from plasma created by CO$_2$ laser with intensity of 10^{11} W/cm^2.

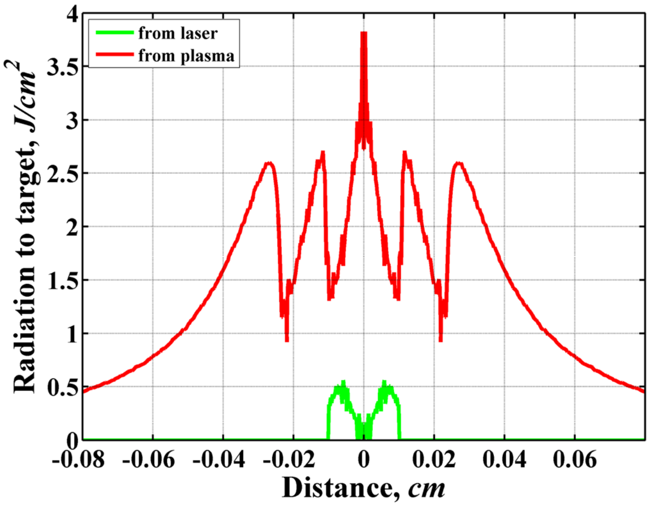

FIG. 8. Radiation to the target from laser and from plasma created by Nd:YAG laser with intensity of 10^{11} W/cm^2.

While accurate modeling of radiation transport in full energy range is critical for understanding plasma evolution to optimize LPP source, calculation of radiation output in the EUV region requires precise atomic data with detailed resolution of spectra in this energy range. We used separate additional detailed optical coefficients for the simulation of EUV photons emission, absorption, and final collection in the 13.5% ± 1% nm range. This significantly increased the accuracy of calculating the important conversion efficiency in the LPP lithography devices. Figures 9 and 10 show the difference in EUV source location and power density of EUV photons collected in 2π sr from plasma heated by the CO$_2$ laser with different initial plasma conditions. In the first case,

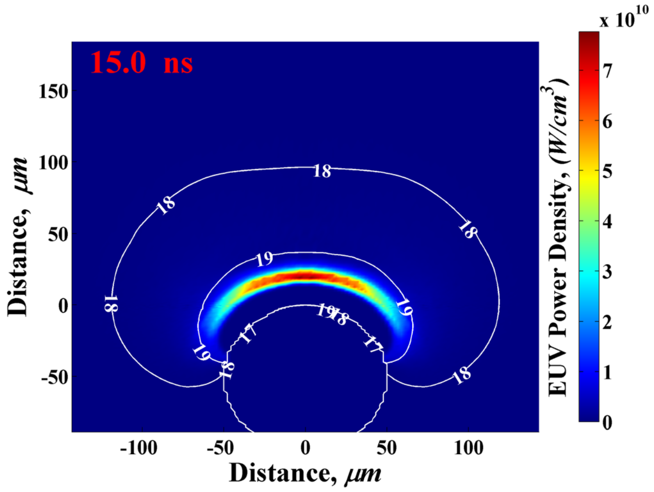

FIG. 9. EUV source strength and location from 100 μm droplet without prepulse; CO$_2$ laser with 300 μm spot and 30 ns pulse.

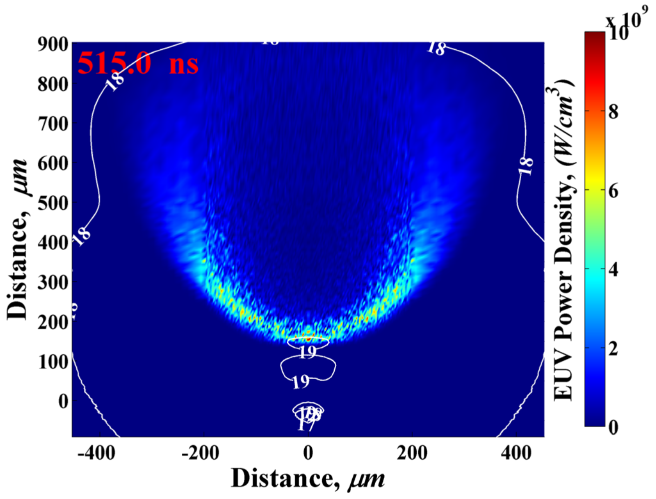

FIG. 10. EUV source strength and location due to pre-plasma created from 50 μm droplet and expanded during 500 ns; CO_2 laser with 300 μm spot and 30 ns pulse.

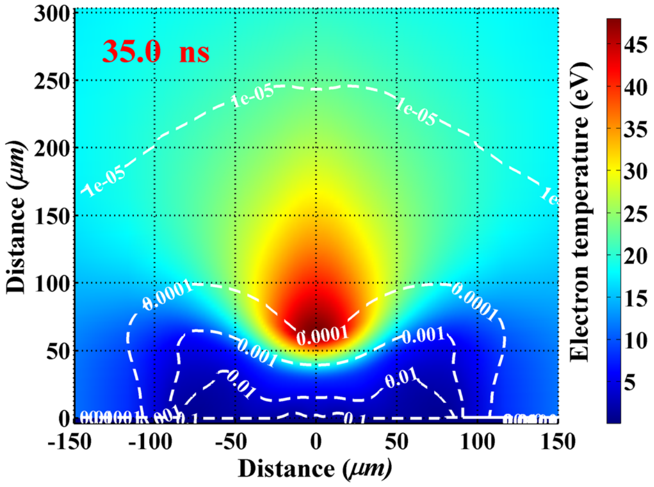

FIG. 11. Electron temperature and mass density (g/cm^3) distribution at 35 ns in plasma created from Sn foil by the CO_2 laser with 30 μm spot (1% CE).

plasma was created in vacuum chamber from droplet using single CO_2 laser during 15 ns of exposure (Fig. 9). In the second case, plasma was prepared using pre-pulse laser, expanded during 500 ns, and then heated by main laser during 15 ns (Fig. 10). Larger plasma plume allowed efficient coupling/utilization of laser energy and extended the area for EUV photons emission. Even higher intensity of EUV power from the single pulse did not compensate for the EUV collection from larger volume. We obtained less than 1% CE from single pulse and more than 3% in the second case. Reducing spot size to match the droplet diameter did not significantly increase the efficiency of single CO_2 devices.

V. HYDRODYNAMIC CONFINEMENT

Hydrodynamic plasma evolution also requires accurate description and precise modeling especially in the simulation of smaller laser spots and targets. The difference in combination of plasma density and temperature in most EUV emissive areas and in surrounding plasma determines photon source efficiency. Distribution of these parameters depends also on hydrodynamic expansion and confinement, which can be controlled by lasers,[18,19] target geometry,[20] or a combination of both.

For example, the CE of LPP sources using small droplets heated by the CO_2 laser is very low, does not exceed 0.5%. This was shown in experiments[21] and in our modeling analysis.[7] Planar targets yield two times higher CE for the same CO_2 laser parameters, i.e., 1% (planar) vs. 0.45% (spherical). The low efficiency even for planar target in this case is due to the very small spot size used. Comparative analysis of plasma temperature and mass density distribution (Figs. 11 and 12) also shows larger potential area for EUV photons emission in the planar target geometry. Increasing droplet size, e.g., to 100 μm, using the same laser parameters given above allowed slight increase in CE, up to 0.6%, that is still lower than for planar target and can be explained due to the combined effect of low plasma confinement for the given geometry and the low efficiency of the CO_2 laser with the considered spot size (Fig. 13). Figure 14 shows the

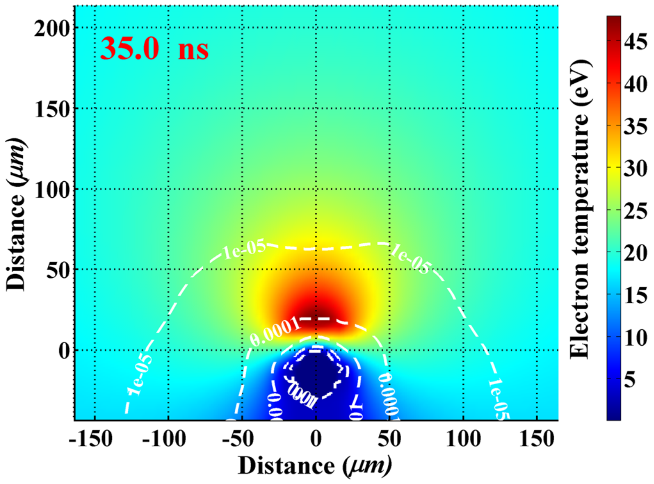

FIG. 12. Electron temperature and mass density (g/cm^3) distribution at 35 ns in plasma created from 30 μm droplet by the CO_2 laser with 30 μm spot (0.45% CE).

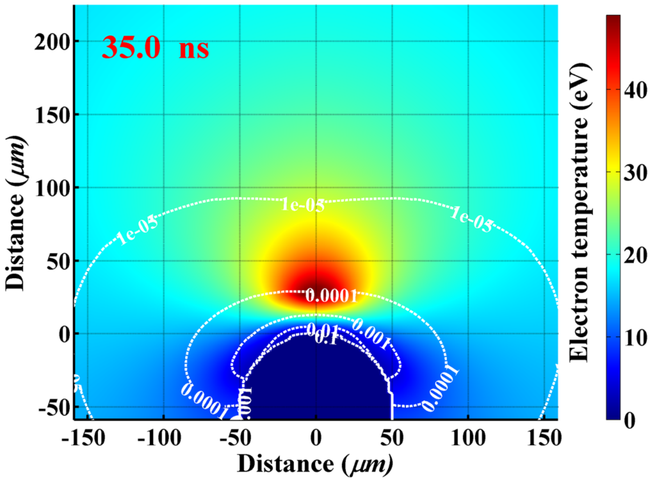

FIG. 13. Electron temperature and mass density (g/cm^3) distribution at 35 ns in plasma created from 100 μm droplet by the CO_2 laser with 30 μm spot (0.6% CE).

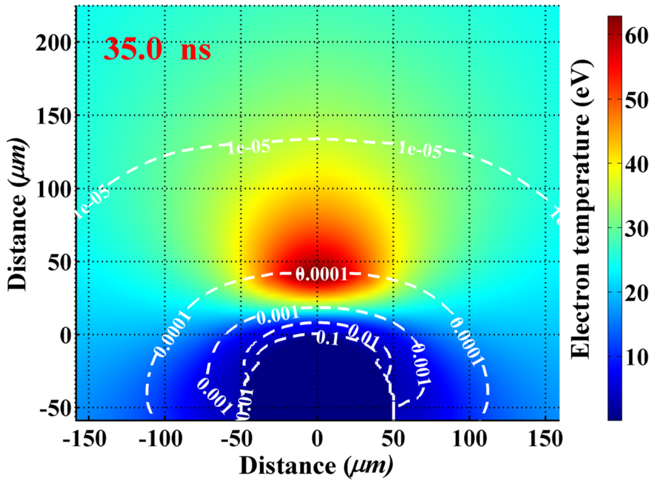

FIG. 14. Electron temperature and mass density (g/cm^3) distribution at 35 ns in plasma created from 100 μm droplet by the CO_2 laser with 50 μm spot (0.9% CE).

distribution of plasma temperature and mass density for the case with larger laser spot size but the same intensity and duration were utilized. Such increase in the laser spot size together with the larger target surface allowed having the CE comparable to that of the planar geometry. All simulations described in this section utilized the CO_2 laser with 30 ns pulse (FWHM) and 5×10^{10} W/cm^2 intensity.

VI. CONCLUSION

We studied the effect of various processes on plasma evolution in LPP sources with regard to the conversion efficiency of these sources for emission and collection of EUV power. Radiation transport and hydrodynamic processes play critical role in determining the conversion efficiencies of laser-produced plasma for EUV sources. Correct simulation of such complex hydrodynamic flow near target surfaces should take into account various energy input from the laser source, i.e., absorption/reflection in solid/liquid target, in target vapor, and in plasma layer. Calculation of radiation output in the EUV region also requires accurate atomic data with detailed resolution of spectra in this energy range. HEIGHTS integrated models in full 3D geometry were extensively benchmarked against various experimental results in various fields of science. Comprehensive integrated computer simulation can, therefore, be used with confidence to simulate and optimize EUV sources for advanced lithography and reduce the need for numerous expensive experiments to identify regimes where optimum target/laser system can be designed.

ACKNOWLEDGMENTS

This work was partially supported by National Science Foundation, PIRE grant. We gratefully acknowledge the computing resources provided by the Fusion cluster operated by the Laboratory Computing Resource Center at Argonne National Laboratory.

[1] V. Sizyuk, A. Hassanein, V. Morozov, and T. Sizyuk, Report No. ANL-MCS-CPH-06/56, Argonne National Laboratory, 2006.
[2] V. Y. Banine, K. N. Koshelev, and G. H. P. M. Swinkels, J. Phys. D: Appl. Phys. **44**, 253001 (2011).
[3] R. C. Spitzer, T. J. Orzechowski, D. W. Phillion, R. L. Kauffman, and C. Cerjan, J. Appl. Phys. **79**, 2251 (1996).
[4] S. Fujioka, M. Shimomura, Y. Shimada, S. Maeda, H. Sakaguchi, Y. Nakai, T. Aota, H. Nishimura, N. Ozaki, A. Sunahara, K. Nishihara, N. Miyanaga, Y. Izawa, and K. Mima, Appl. Phys. Lett. **92**, 241502 (2008).
[5] J. R. Freeman, S. S. Harilal, A. Hassanein, and B. Rice, Appl. Phys. A **110**, 853 (2013).
[6] K. Nishihara, A. Sunahara, A. Sasaki, M. Nunami, H. Tanuma, S. Fujioka, Y. Shimada, K. Fujima, H. Furukawa, T. Kato, F. Koike, R. More, M. Murakami, T. Nishikawa, V. Zhakhovskii, K. Gamata, A. Takata, H. Ueda, H. Nishimura, Y. Izawa, N. Miyanaga, and K. Mima, Phys. Plasmas **15**, 056708 (2008).
[7] T. Sizyuk and A. Hassanein, J. Appl. Phys. **112**, 033102 (2012).
[8] T. Sizyuk and A. Hassanein, Phys. Plasmas **19**, 083102 (2012).
[9] S. S. Harilal, T. Sizyuk, A. Hassanein, D. Campos, P. Hough, and V. Sizyuk, J. Appl. Phys. **109**, 063306 (2011).
[10] A. Hassanein, V. Sizyuk, T. Sizyuk, and S. S. Harilal, J. Micro/Nanolith. MEMS MOEMS **8**, 041503 (2009).
[11] A. Hassanein and T. Sizyuk, Phys. Plasmas **20**, 053105 (2013).
[12] A. Hassanein, T. Sizyuk, V. Sizyuk, and S. S. Harilal, J. Micro/Nanolith. MEMS MOEMS **10**, 033002 (2011).
[13] S. R. Goldman and R. F. Schmalz, Phys. Fluids **30**, 3608–3615 (1987).
[14] A. Hassanein, G. L. Kulcinski, and W. G. Wolfer, Nucl. Eng. Des. Fusion **1**, 307–324 (1984).
[15] V. Tolkach, V. Morozov, and A. Hassanein, Report No. ANL-ET/02-23, Argonne National Laboratory, 2002.
[16] V. Morozov, V. Tolkach, and A. Hassanein, Report No. ANL-ET-04/24, Argonne National Laboratory, 2004.
[17] G. Cisneros, J. S. Helman, and C. N. J. Wagner, Phys. Rev. B **25**, 4248–4251 (1982).
[18] V. Sizyuk, A. Hassanein, and T. Sizyuk, J. Appl. Phys. **100**, 103106 (2006).
[19] V. Sizyuk, A. Hassanein, and T. Sizyuk, Laser Part. Beams **25**, 143–154 (2007).
[20] S. S. Harilal, T. Sizyuk, V. Sizyuk, and A. Hassanein, Appl. Phys. Lett. **96**, 111503 (2010).
[21] H. Mizoguchi, T. Abe, Y. Watanabe, T. Ishihara, T. Ohta, T. Hori, T. Yanagida, H. Nagano, T. Yabu, S. Nagai, G. Soumagne, A. Kurosu, K. M. Nowak, T. Suganuma, M. Moriya, K. Kakizaki, A. Sumitani, H. Kameda, H. Nakarai, and J. Fujimoto, Proc. SPIE **7969**, 796908 (2011).